Two-Photon Excitation and Photoconversion of EosFP in Dual-Color 4Pi Confocal Microscopy

Sergey Ivanchenko,* Sylvia Glaschick,* Carlheinz Röcker,* Franz Oswald,[†] Jörg Wiedenmann,[‡] and G. Ulrich Nienhaus*[§]

*Institute of Biophysics, [†]Department of Internal Medicine I, and [‡]Institute of General Zoology and Endocrinology, University of Ulm, 89069 Ulm, Germany; and [§]Department of Physics, University of Illinois at Urbana-Champaign, Urbana, Illinois 61801

ABSTRACT   Recent years have witnessed enormous advances in fluorescence microscopy instrumentation and fluorescent marker development. 4Pi confocal microscopy with two-photon excitation features excellent optical sectioning in the axial direction, with a resolution in the 100 nm range. Here we apply this technique to cellular imaging with EosFP, a photoactivatable autofluorescent protein whose fluorescence emission wavelength can be switched from green (516 nm) to red (581 nm) by irradiation with 400-nm light. We have measured the two-photon excitation spectra and cross sections of the green and the red species as well as the spectral dependence of two-photon conversion. The data reveal that two-photon excitation and photoactivation of the green form of EosFP can be selectively performed by choosing the proper wavelengths. Optical highlighting of small subcellular compartments was shown on HeLa cells expressing EosFP fused to a mitochondrial targeting signal. After three-dimensionally confined two-photon conversion of EosFP within the mitochondrial networks of the cells, the converted regions could be resolved in a 3D reconstruction from a dual-color 4Pi image stack.

INTRODUCTION

Fluorescence microscopy has acquired a key role in life science research in recent years due to its ability to image the cellular interior in a noninvasive, three-dimensional (3D) fashion using confocal detection and/or multiphoton excitation. Significant advances have been made in improving the spatial resolution, including coherent wavefront superpositions in 4Pi (1,2) and I^5M (3) schemes and sophisticated approaches exploiting reversible saturable fluorescence transitions, whereby an effective point spread function (PSF) of subdiffraction size can be achieved (4).

This development in fluorescence microscopy was further spurred by the widespread application of genetically encoded fluorescent marker proteins (FPs). They can be fused to almost any target protein at the DNA level and thus are powerful tools for probing gene expression, protein localization, or protein-protein interaction in the cellular environment. Exciting new possibilities have emerged from the advent of photoactivatable FPs (5). These optical marker proteins allow the fluorescence emission intensity or color to be controlled by irradiation with light at specific wavelengths (6–10). We have recently identified and characterized EosFP, a protein that can be irreversibly switched from green to red emission by illumination with ~400-nm light, which induces a photochemical modification of the chromophore (10–12). Photoactivatable proteins have been recognized as key tools with which to achieve subdiffraction imaging (13,14) and, moreover, they enable localized photoactivation in subcellular

regions and subsequent in vivo tracking of the marked proteins. In standard fluorescence microscopy using one-photon excitation (OPE), the optically marked region is limited by the size of the illuminating laser spot in the lateral dimensions, but there is no selective photoactivation along the axial dimension. However, confinement in all three spatial dimensions is possible by using two-photon activation (TPA), as shown for the photoactivatable proteins PA-GFP (15), KikG (16), and EosFP (17).

3D imaging of subcellular territories requires high resolution in all three dimensions, which can be achieved by optical sectioning using confocal or multiphoton microscopy. Here again, the axial dimension is the most critical, with a resolution three to four times lower than in the image plane. To improve the axial resolution, 4Pi confocal microscopy was introduced, featuring a coherent superposition of two spherical wavefronts by means of two opposing lenses (1). 4Pi microscopy types A, B, and C are distinguished, depending on the coherent superposition of the exciting light, emitted light, or both, respectively. Over the years, Hell and co-workers have developed 4Pi confocal microscopy into a reliable technique for high resolution optical microscopy (2,18–21), and a commercial instrument (Leica TCS 4Pi) has recently become available. In 4Pi microscopy, the opposing wavefronts generate an interference pattern along the axial direction that consists of a sharp central maximum with a full width at half-maximum of ~100 nm and a series of side lobes due to the incomplete solid angle of the interfering waves. A combination of strategies is pursued to achieve sufficient suppression of the interference side lobes. In 4Pi microscopy of type A, confocal detection and two-photon excitation (TPE) are usually employed in conjunction. Thereby, the side lobes can be suppressed to <25% of the main peak,

---

which enables reliable image reconstruction by deconvolution. The resulting axial resolution of ~100 nm is excellent for 3D tracking of protein subpopulations carrying a photo-activated label.

In this study, we have combined 3D optical marking of subcellular regions and 4Pi confocal microscopy using EosFP. Efficient TPE in 4Pi microscopy and TPA for 3D-localized optical marking require a thorough characterization of the respective nonlinear properties of the marker protein. Therefore, we have measured the spectral dependencies of TPA and TPE of the green form of EosFP as well as the TPE cross sections for both the green and the red forms. This knowledge allowed us to select optimal imaging parameters in a cellular application using EosFP fused to a mitochondrial targeting signal in HeLa cells. After two-photon conversion of a small subregion within the mitochondrial network of HeLa cells, the photoactivated volume was resolved in a 3D reconstruction from a dual-color 4Pi image stack.

MATERIALS AND METHODS

Characterization of two-photon excitation and conversion of EosFP

Experiments were performed on a homebuilt apparatus based on a Zeiss Axiovert 35 inverted microscope (Carl Zeiss, Jena, Germany) equipped with a P-731.20 piezoelectric scanning stage (Physik Instrumente, Karlsruhe, Germany). Linearly polarized light from an Ar^+ ion laser pumped femto-second Ti:Sapphire laser (Innova Sabre/Mira 900, Coherent, Santa Clara, CA) was used for TPE and TPA of the green form of EosFP, employing two different laser mirror sets (780–920 nm and 900–1050 nm). Spectral band-width, center wavelength, and pulse duration of the laser emission were characterized by using a spectrometer (PulseCheck, APE, Berlin, Germany) and an autocorrelator (Wavescan, APE). TPE of the red form of EosFP was performed at 1064 nm with a picosecond Nd:YVO$_4$ laser (GE-100-VAN-IR/SHG, Time-Bandwidth Products, Zürich, Switzerland), running at a pulse repetition rate of 40 MHz. For OPE of EosFP, we used 488-nm continuous wave radiation from an Ar^+/Kr^+ ion laser (modified model 164, Spectra Physics, Mountain View, CA), which was combined with the pulsed infrared light on a dichroic mirror (640 DCSPXR, AHF, Tübingen, Germany). Both infrared and visible excitation wavelengths were reflected by a suitable dichroic mirror (FF495-Di02, Semrock, Rochester, NY) before entering the objective lens. We took a water immersion objective C-Apochromat 63×/1.20 W Korr (Zeiss) for measurements on different samples at a single excitation wavelength and an oil immersion objective Plan-Neofluar 63×/1.25 Oil (Zeiss) for wavelength-dependent experiments because of its much weaker spectral dependence in the infrared region. The emitted fluorescence was spectrally separated by a dichroic mirror 560 DCXR (AHF) and passed through two emission filters—HQ 535/70 (AHF) and HQ 610/75 (AHF)—so that photons were separately registered in a green (500–570 nm) and a red (572–648 nm) spectral channel by two avalanche photodiodes (APDs; SPCM-AQR-14, Perkin-Elmer, Vaudreuil, Quebec, Canada).

For the determination of TPE cross sections of the green and red forms of EosFP, fluorescein and rhodamine 6G were used as reference dyes, with TPE cross sections reported as 26 GM (1 GM = 10^{-50} cm^4 s) at 920 nm (22) and 3.6 GM at 1064 nm (23,24), respectively. To account for the spectral dependencies of the pulse duration, $\Delta\tau \propto \lambda^2/\Delta\lambda$, and the excited volume, $V \propto \lambda^3$, the excitation powers were corrected according to

$$P_{corr} = \frac{\lambda_{ref}^5 \Delta\lambda}{\lambda^5 \Delta\lambda_{ref}} P_{exp}. \quad (1)$$

Here, the reference values were taken at 920 nm; P_{exp} is the measured laser power. For the wavelength-dependent TPA experiments with EosFP on surfaces, the power density was corrected according to the diffraction-limited illuminated area, $S \sim \lambda^2$. The laser pulse duration was kept constant at 160 fs throughout the wavelength range.

4Pi microscopy

TPA of EosFP in cells with subsequent 4Pi imaging was performed on a commercial 4Pi microscope with TPE (Leica TCS 4Pi, Leica Microsystems, Mannheim, Germany), using a matched pair of opposing objective lenses (HCX PL APO 100×/1.35 GLYC CORR CS, Leica Microsystems) to achieve a coherent superposition of two exciting wavefronts (4Pi type A). For TPE of EosFP, the picosecond Ti:Sapphire laser (Mai Tai, Spectra Physics) was tuned to 970 nm, whereas TPA was performed at 810 nm. 4Pi image stacks were recorded as y-stacked xz-scans with a typical voxel size of 15 × 15 × 30 nm in a green (500–530 nm) and a red (572–648 nm) spectral channel, using APD detectors. The pinhole size was set to 1 airy unit, and bidi-rectional scans were performed with a scanning rate of 400 lines per second. Eight lines were averaged; frame accumulation was set to 2–4. For photo-conversion, a particular spot within the cell was illuminated for 20 s with an excitation power of 1.6 mW at the entrance of the microscope, corresponding to ~80 μW at the sample (upper objective only). Image processing was limited to blurring, cross talk correction, and a one-dimensional linear three-point deconvolution with the ImSpector software package (25). This procedure removes side lobe artifacts without introducing any resolution enhancement. After rescaling, overlays were generated from the images of the red and the green channels. Volume rendering of the image stacks was performed using the program Voxx (26).

Sample preparation

EosFP was expressed in *Escherichia coli* (BL21 DE3) and purified as de-scribed (17). For the spectroscopic experiments, the sample was prepared in a sandwich of two glass coverslips separated by Mylar foils. TPE experi-ments were performed with micromolar concentrations of EosFP dissolved in 100 mM sodium phosphate buffer at pH 7. Solutions of fluorescein (Sigma-Aldrich, Seelze, Germany) at pH 11 and rhodamine 6G (Lambda Physik, Göttingen, Germany) in methanol were used as reference standards. TPA experiments were performed on a dense layer of EosFP immobilized on a bovine serum albumin (BSA) coated surface via biotin-streptavidin coupling (17).

For 4Pi microscopy, HeLa cells (ATCC CCL 2) were grown at 37°C under 5% CO$_2$ in Dulbecco's modified Eagle's medium (Gibco, Karlsruhe, Germany) supplemented with 10% fetal calf serum. A total of 2 × 10^5 cells was plated on circular quartz coverslips (Leica) in 6-cm diameter dishes. After 16 h, the cells were transfected with 2 μg of the expression vector pcDNA3-mt-EosFP using the FuGENE transfection reagent (Roche, Mannheim, Ger-many). In this vector, cDNA coding for EosFP is fused to cDNA coding for the mitochondrial (mt) targeting signal from subunit VIII of cytochrome *c* oxidase (10). By means of this targeting sequence, the expressed protein, mt-EosFP, localizes in the mitochondria of transfected HeLa cells. Cells were rinsed with phosphate buffered saline (PBS; Gibco) 24 h after transfec-tion and fixed with 4% paraformaldehyde (PFA, Merck, Darmstadt, Germany) for 10 min at room temperature. Sandwiches of two coverslips were as-sembled with PBS/glycerol (13%:87%, v/v) as a mounting medium. All experiments were carried out in temperature-controlled laboratories at 22°C.

RESULTS AND DISCUSSION

Two-photon excitation of EosFP

We have performed a thorough determination of the spectral dependence of TPE of the green form of EosFP across the

entire excitation band 800–1050 nm, as shown in Fig. 1. Particular attention was paid to the range above 1000 nm, which required a delicate alignment of the Ti:Sapphire laser. To ensure that photobleaching and saturation had no influence on the data, the linear dependence of the fluorescence intensity on the squared excitation power was confirmed at each wavelength (Fig. 1, *inset*). TPE cross sections were determined from the resultant slopes of the linear parts of the curves,

$$\delta_1 = \frac{\text{slope}_1}{\text{slope}_2} \times \frac{c_2 \Phi_2 \eta_2}{c_1 \Phi_1 \eta_1} \times \delta_2. \qquad (2)$$

By using Eq. 2, we account for the effects of different concentrations (c), quantum yields (Φ), and spectral detection efficiencies (η) of the sample (subscript ''1'') and a reference solution of known TPE cross section (subscript ''2''). Using fluorescein as a reference, the TPE cross section of the green form of EosFP was determined as 2.0 ± 0.5 GM at 920 nm. All wavelength-dependent TPE determinations were scaled to this value, including corrections for the spectral dependencies of spot size and pulse duration. The TPE spectrum of the green form of EosFP in Fig. 1 shows a maximum cross section of 19 ± 5 GM at the wavelength of 1000 ± 5 nm, which lies in the range reported for other autofluorescent proteins (27,28). Comparison of the spectral shapes of OPE (plotted at twice the wavelength) and TPE yields a blue shift of 12 nm for the maximum, which corresponds to an energy shift by 120 cm^{-1}. This displacement between the OPE and TPE peaks is by a factor of six larger in EGFP and twice larger in ECFP (28). For some fluorophores, much larger shifts have been observed; for example, the TPE spectrum of tyrosine is displaced by 2000 cm^{-1} from its OPE spectrum (29).

The TPE spectrum of EosFP displays vibronic structure, most prominently a well-resolved vibronic band at ~940 nm, whereas the corresponding OPE spectrum shows only a shoulder. An exact coincidence of the spectra is not expected because the selection rules for OPE and TPE are different, and the two types of electronic transition are likely coupled to different vibrational modes (28–30), as is also apparent from the different vibronic features in the OPE and TPE spectra of EosFP in Fig. 1.

The TPE spectrum of the red form of EosFP is expected to have a maximum at ~1150 nm. No laser is available in our laboratory to cover this range; and, therefore, we determined the TPE properties of the red form of EosFP only at 1064 nm, a laser wavelength used by many laboratories. For comparison, we have also studied TPE of eqFP611, a far-red fluorescent protein which we have investigated recently (31–33). Fig. 2 shows the dependence of the fluorescence intensity on the squared power for the two autofluorescent proteins and our reference sample, rhodamine 6G. Sublinear behavior is noticeable at higher powers due to ground state depletion, blinking, and photobleaching. Therefore, we only took the data below 20 mW to determine the slopes. By referencing them to rhodamine 6G, we obtained TPE cross sections of 4.2 ± 0.3 GM for eqFP611 and 5.0 ± 0.4 GM for the red form of EosFP.

Two-photon conversion of EosFP

To characterize the power and spectral dependencies of the TPA efficiency, a dense surface layer of EosFP was scanned in one dimension with a focused infrared beam at a velocity of a few micrometers per second to locally photoconvert proteins from the green to the red form. Several lines were drawn next to each other using different laser intensities and wavelengths. Subsequently, an image was scanned with 488-nm excitation, and a set of lines appeared in the red detection channel due to EosFP molecules that were red converted
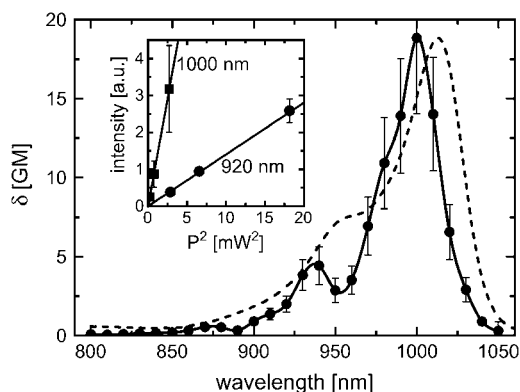

FIGURE 1 TPE spectrum of the green form of EosFP (*dots* and *solid line*) and OPE spectrum with wavelengths doubled for comparison (*dashed line*). The error bars in the TPE spectrum mainly represent the uncertainty of the TPE cross sections of the fluorescein reference; the relative error between different points within the spectrum did not exceed 6%. The inset shows the linear dependence of the fluorescence intensity on the square of the excitation power at two representative wavelengths.
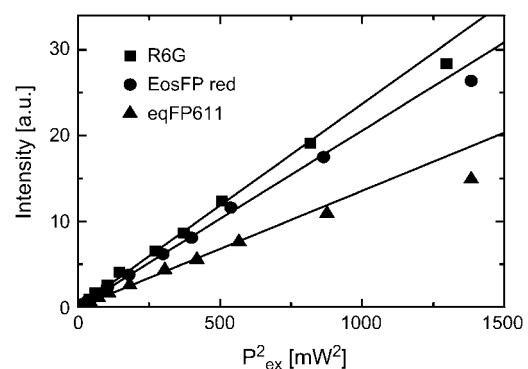

FIGURE 2 Fluorescence intensity versus squared excitation power at 1064 nm for the red form of EosFP (*circles*), eqFP611 (*triangles*), and the reference standard rhodamine 6G (*squares*). The straight lines are linear fits to the power range below 20 mW.

with 800-nm light at different excitation powers between 1 and 7.5 mW (Fig. 3 A) or infrared light between 800 and 880 nm in 10-nm steps at a constant power density of 1.8 MW/cm^2 (Fig. 3 B). Vertically averaged profiles (Fig. 3, *lower panels*) were used for the quantitative analysis. They were fitted with Gaussians of identical widths, and the heights were taken to reflect the power and spectral dependencies of the TPA yield. The dependence of the conversion yield at 800 nm is shown in Fig. 4 A as a function of the squared average power.

With only a few milliwatts, significant photoactivation can already be achieved, and a linear dependence on the squared power is observed, as indicated by the dashed line. Toward higher average powers, the conversion yield saturates due to the locally limited number of convertible fluorophores and photobleaching. Neglecting the latter effect, an exponential saturation function is expected for the density of converted molecules, $C(P^2) = C_{sat}(1 - \exp(-P^2/P_{sat}^2))$, where the saturation amplitude, C_{sat}, depends on the total density of fluorophores in the sample, and the saturation power, P_{sat}, reflects the inverse two-photon conversion cross section under the given experimental conditions. The solid line in Fig. 4 A represents a fit of the model to the data, which yields a saturation power of $P_{sat} = 3.7$ mW. This value is well below the power limit of ~10 mW, above which damage was reported to become significant in live cell imaging (34). Fig. 4 B shows the wavelength dependence of TPA after correction for the spectral dependence of the spot size. Within the measured wavelength range, TPA is maximal at 790 nm and decreases toward 900 nm.

This behavior coincides with the expectation from the one-photon photoconversion action spectrum of EosFP, which is tightly associated with the protonated state (10,11). Interestingly, a shoulder appears in the TPA spectrum at 830 nm, which closely matches the wavelength of three-photon excitation of aromatic amino acids. It is known that the EosFP chromophore can be efficiently excited at 280 nm via resonance energy transfer (10), and the shoulder at 830 nm in Fig. 4 B suggests that photoactivation can also occur by excitation of aromatic amino acids near the chromophore. From a practical point of view, wavelengths below 800 nm are less attractive for TPA, as they bear an increasing risk of additional one-photon processes even for weak transitions due to the rather high powers applied. The increased multiphoton absorption of the surrounding protein matrix may also lead to deviations from the expected spectral shape below 800 nm, as was found for the TPA of PA-GFP (15).

4Pi microscopy and 3D localized optical marking with EosFP

In Fig. 5, we compare images of mitochondria from a HeLa cell transfected with mt-EosFP in an *xz* projection. The 3D PSF in conventional two-photon confocal microscopy has the shape of an ellipsoid that is strongly elongated in the axial direction and does not allow objects to be resolved that are closer than ~500–800 nm in the axial direction. By contrast, 4Pi confocal microscopy has an excellent axial resolution and is clearly capable of resolving mitochondrial structures in great detail. Interconnections and gaps between the tubular structures, which are completely obscured in conventional confocal microscopy with 488-nm OPE (Fig. 5 A), can be discerned in the 970-nm TPE 4Pi image of the same region after deconvolution (Fig. 5 B). 4Pi microscopy thus enables 3D image reconstructions of mitochondrial networks with comparable resolution in all three spatial dimensions using the Leica TCS 4Pi.

Inspection of Figs. 1 and 4 B indicates that it may be possible to achieve TPA and TPE of EosFP independently from each other by selecting a wavelength near 1000 nm for excitation and a wavelength near 800 nm for activation. We chose an excitation wavelength of 970 nm for 4Pi imaging as
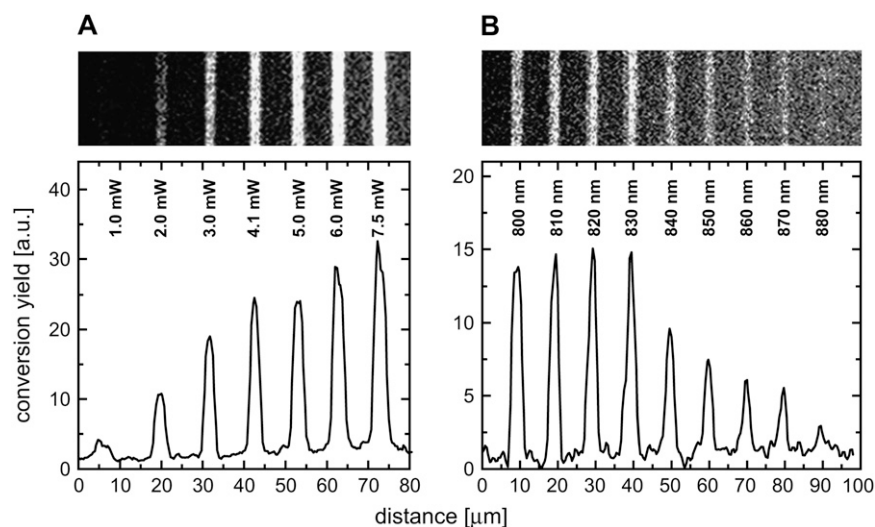
FIGURE 3 Two-photon conversion of EosFP immobilized on a BSA surface. Lines of red-converted protein were drawn using (*A*) 800-nm illumination at average powers between 1 and 7.5 mW (scan velocity 2.3 μm/s) and (*B*) different wavelengths from 800 nm to 880 nm in 10-nm steps at a constant power density of ~1.8 MW/cm^2 (scan velocity 4.7 μm/s). The red form of EosFP thereby produced was detected in a subsequent scan with 488-nm illumination. Vertically averaged profiles of the lines after cross talk subtraction are shown in the two lower panels.
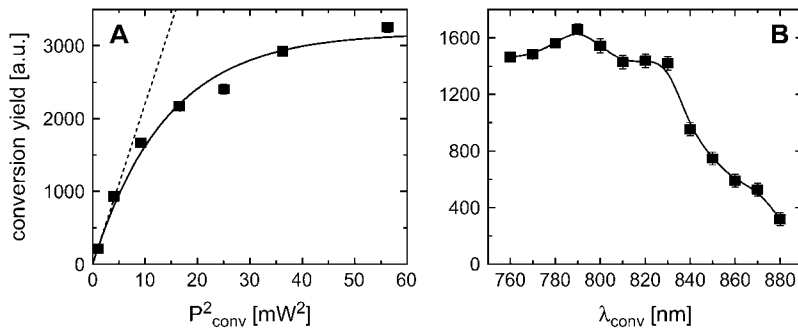
FIGURE 4 Analysis of the TPA data on EosFP as a function of excitation power and wavelength. (*A*) Power dependence at $\lambda = 800$ nm, the solid line represents a fit of an exponential saturation curve to the data, and the dashed line indicates the linear term of its power series. (*B*) Spectrum of conversion yields; the solid line is drawn to guide the eye.

a compromise between excitability and laser gain profile. At this wavelength, photoconversion was not detectable. With irradiation at 810 nm, however, pronounced red conversion is easily achieved in cellular samples, as demonstrated by the images of a HeLa cell transfected with mt-EosFP in Fig. 6. A particular spot in the cell was irradiated for 20 s using only the upper objective of the 4Pi microscope to obtain a locally confined, smooth volume of photoconverted molecules without the fringe structure of coherent excitation by two objectives. Subsequently, 4Pi image stacks were recorded with simultaneous acquisition in both the green and the red detection channels. Fig. 6 *A* displays the *xz* projection of an image stack as an overlay of both channels after applying cross talk correction and linear point deconvolution. In this example, EosFP molecules in two mitochondrial tubules separated by <500 nm in the axial direction were photoconverted. The photoactivation volume is represented by the white ellipse scaled by the lateral and axial 1/e radii of the squared illumination PSF (35); hence it also shows the approximate spatial resolution that can be achieved using standard nonconfocal TPE microscopy. The TPE selectivity is excellent but not sufficient, though, to address individual mitochondria in the axial direction. In Fig. 6, *B* and *C*, we show further 4Pi images with localized TPA. Two projections are displayed that were obtained by volume rendering of the 3D image data (a complete 3D reconstruction is available as a movie in the Supplementary Material).

These examples clearly demonstrate the capabilities of 4Pi microscopy in applications using photoactivatable optical markers such as EosFP for high resolution optical imaging of cellular processes. However, the excitation wavelengths and

powers have to be carefully controlled to avoid local two-photon photobleaching due to the nonlinear nature of the two-photon processes involved. The experiments can be further optimized in a variety of ways. Red-converted proteins can be more efficiently excited by using laser sources emitting further into the infrared region. The performance of 4Pi microscopy on fixed samples can be further advanced by
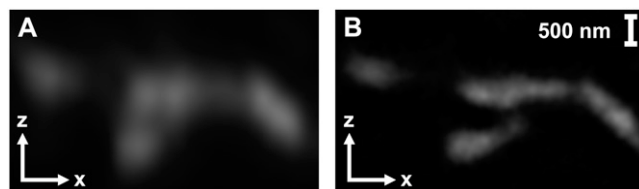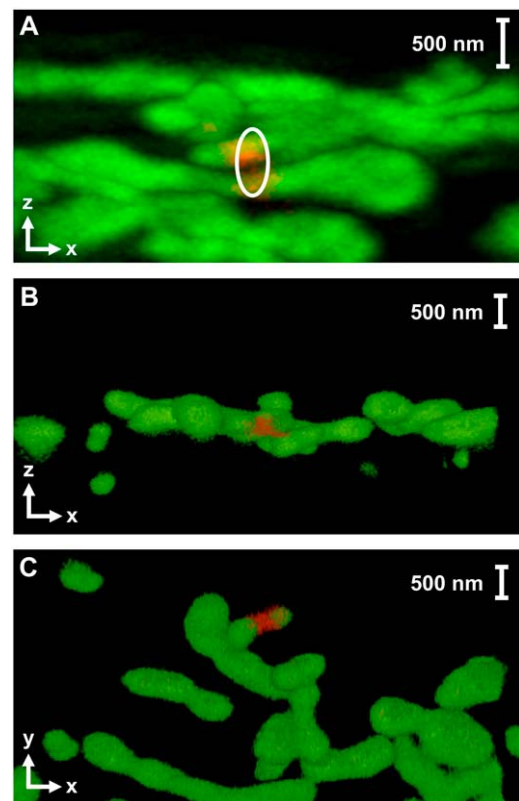

FIGURE 6 4Pi two-photon microscopy images of EosFP-labeled mitochondrial networks, excited at 970 nm, showing 3D-localized TPA with 810-nm light. (*A*) Axially densely packed network structures in *xz* projection, well resolved by 4Pi microscopy. The size of the TPA volume, based on the 1/e radii of the squared illumination PSF, is shown as a white ellipsoid, with radial and axial dimensions of 290 and 670 nm. Volume-rendered 3D reconstruction of a network shown as a projection in (*B*) the *xz* plane and (*C*) the *xy* plane. The complete 3D reconstruction of the image stack is available as a movie in the Supplementary Material.

FIGURE 5 Comparison of the resolution in the *xz* plane of standard confocal and 4Pi microscopy images of a section of the mitochondrial network in a HeLa cell labeled with mt-EosFP. (*A*) Confocal image (excitation at 488 nm) and (*B*) 4Pi image (TPE at 970 nm, three-point deconvolution applied).

usage of high numerical aperture oil objective lenses in combination with a novel tunable mounting medium (36) instead of the glycerol objective lenses that we currently use on fixed cell preparations. Live cell imaging at ultra high resolution, however, requires water objectives. Their alignment is more demanding, and avoiding phase shifts due to refractive index mismatch becomes even more challenging. An active compensation circuit for the phase shifts within the sample will be useful to implement (37). Alternatively, sophisticated deconvolution algorithms can be applied to remove the effects of phase shifts from the image (38).

CONCLUSIONS

4Pi confocal microscopy in combination with photoactivatable, autofluorescent proteins such as EosFP offers great potential for high resolution cellular imaging, and ongoing advances in both fluorescent marker and instrument design will further help simplify the procedures. To assess EosFP's capabilities in these applications, we have carried out thorough characterizations of TPE of the green and red forms of EosFP and of TPA for switching the protein from green to red emission. As a simple demonstration, we have studied the mitochondrial network of HeLa cells labeled with EosFP by means of transfection with DNA coding for a fusion construct of EosFP and a mitochondrial targeting signal. The experiments show that TPE and TPA of EosFP can be completely uncoupled by an appropriate choice of wavelengths, allowing molecules in a small volume within the cell to be addressed and switched from green to red emission. In the future, we will employ this technique for tracking the red-converted EosFP in live cell imaging applications at ultra high resolution.

SUPPLEMENTARY MATERIAL

An online supplement to this article can be found by visiting BJ online at http://www.biophysj.org.

REFERENCES

1. Hell, S. W., and E. H. K. Stelzer. 1992. Fundamental improvement of resolution with a 4Pi-confocal fluorescence microscope using two-photon excitation. *Opt. Commun.* 93:277–282.

2. Egner, A., and S. W. Hell. 2005. Fluorescence microscopy with super-resolved optical sections. *Trends Cell Biol.* 15:207–215.

3. Gustafsson, M. G., D. A. Agard, and J. W. Sedat. 1995. Sevenfold improvement of axial resolution in 3D widefield microscopy using two objective lenses. *Proc. SPIE.* 2412:147–156.

4. Hofmann, M., C. Eggeling, S. Jakobs, and S. W. Hell. 2005. Breaking the diffraction barrier in fluorescence microscopy at low light intensities by using reversibly photoswitchable proteins. *Proc. Natl. Acad. Sci. USA.* 102:17565–17569.

5. Wiedenmann, J., and G. U. Nienhaus. 2006. Live-cell imaging with EosFP and other photoactivatable marker proteins of the GFP family. *Expert Rev. Proteomics.* 3:361–374.

6. Patterson, G. H., and J. Lippincott-Schwartz. 2002. A photoactivatable GFP for selective photolabeling of proteins and cells. *Science.* 297:1873–1877.

7. Ando, R., H. Mizuno, and A. Miyawaki. 2004. Regulated fast nucleocytoplasmic shuttling observed by reversible protein highlighting. *Science.* 306:1370–1373.

8. Ando, R., H. Hama, M. Yamamoto-Hino, H. Mizuno, and A. Miyawaki. 2002. An optical marker based on the UV-induced green-to-red photoconversion of a fluorescent protein. *Proc. Natl. Acad. Sci. USA.* 99:12651–12656.

9. Chudakov, D. M., V. V. Belousov, A. G. Zaraisky, V. V. Novoselov, D. B. Staroverov, D. B. Zorov, S. Lukyanov, and K. A. Lukyanov. 2003. Kindling fluorescent proteins for precise in vivo photolabeling. *Nat. Biotechnol.* 21:191–194.

10. Wiedenmann, J., S. Ivanchenko, F. Oswald, F. Schmitt, C. Röcker, A. Salih, K. D. Spindler, and G. U. Nienhaus. 2004. EosFP, a fluorescent marker protein with UV-inducible green-to-red fluorescence conversion. *Proc. Natl. Acad. Sci. USA.* 101:15905–15910.

11. Nienhaus, K., G. U. Nienhaus, J. Wiedenmann, and H. Nar. 2005. Structural basis for photo-induced protein cleavage and green-to-red conversion of fluorescent protein EosFP. *Proc. Natl. Acad. Sci. USA.* 102:9156–9159.

12. Nienhaus, G. U., K. Nienhaus, A. Holzle, S. Ivanchenko, F. Renzi, F. Oswald, M. Wolff, F. Schmitt, C. Rocker, B. Vallone, W. Weidemann, R. Heilker, H. Nar, and J. Wiedenmann. 2006. Photoconvertible fluorescent protein EosFP: biophysical properties and cell biology applications. *Photochem. Photobiol.* 82:351–358.

13. Betzig, E., G. H. Patterson, R. Sougrat, O. W. Lindwasser, S. Olenych, J. S. Bonifacino, M. W. Davidson, J. Lippincott-Schwartz, and H. F. Hess. 2006. Imaging intracellular fluorescent proteins at nanometer resolution. *Science.* 313:1642–1645.

14. Hess, S. T., T. P. Girirajan, and M. D. Mason. 2006. Ultra-high resolution imaging by fluorescence photoactivation localization microscopy. *Biophys. J.* 91:4258–4272.

15. Schneider, M., S. Barozzi, I. Testa, M. Faretta, and A. Diaspro. 2005. Two-photon activation and excitation properties of PA-GFP in the 720–920-nm region. *Biophys. J.* 89:1346–1352.

16. Tsutsui, H., S. Karasawa, H. Shimizu, N. Nukina, and A. Miyawaki. 2005. Semi-rational engineering of a coral fluorescent protein into an efficient highlighter. *EMBO Rep.* 6:233–238.

17. Ivanchenko, S., C. Röcker, F. Oswald, J. Wiedenmann, and G. U. Nienhaus. 2005. Targeted green-to-red photoconversion of EosFP, a fluorescent marker protein. *J. Biol. Phys.* 31:249–259.

18. Nagorni, M., and S. W. Hell. 1998. 4Pi-confocal microscopy provides three-dimensional images of the microtubule network with 100- to 150-nm resolution. *J. Struct. Biol.* 123:236–247.

19. Kano, H., S. Jakobs, M. Nagorni, and S. W. Hell. 2001. Dual-color 4Pi-confocal microscopy with 3D-resolution in the 100 nm range. *Ultramicroscopy.* 90:207–213.

20. Egner, A., S. Jakobs, and S. W. Hell. 2002. Fast 100-nm resolution three-dimensional microscope reveals structural plasticity of mitochondria in live yeast. *Proc. Natl. Acad. Sci. USA.* 99:3370–3375.

21. Gugel, H., J. Bewersdorf, S. Jakobs, J. Engelhardt, R. Storz, and S. W. Hell. 2004. Cooperative 4Pi excitation and detection yields sevenfold sharper optical sections in live-cell microscopy. *Biophys. J.* 87:4146–4152.

22. Albota, M. A., C. Xu, and W. W. Webb. 1998. Two-photon fluorescence excitation cross sections of biomolecular probes from 690 to 960 nm. *Appl. Opt.* 37:7352–7356.

23. Bradeley, D. J., M. H. R. Hutchinson, and H. Koetser. 1972. Inter-actions of picosecond laser pulses with organic molecules. II. Two-photon absorption cross-sections. *Proc. R. Soc. Lond. A.* 329:105–119.

24. Kaatz, P., and D. P. Shelton. 1999. Two-photon fluorescence cross-section measurements calibrated with hyper-Rayleigh scattering. *J. Opt. Soc. Am. B.* 16:998–1006.

25. Schönle, A. 2006. ImSpector Image Acquisition and Analysis Software, v0.1. http://www.imspector.de.

26. Clendenon, J. L., C. L. Phillips, R. M. Sandoval, S. Fang, and K. W. Dunn. 2002. Voxx: a PC-based, near real-time volume rendering system for biological microscopy. *Am. J. Physiol. Cell Physiol.* 282:C213–C218.

27. Xu, C., W. Zipfel, J. B. Shear, R. M. Williams, and W. W. Webb. 1996. Multiphoton fluorescence excitation: new spectral windows for biological nonlinear microscopy. *Proc. Natl. Acad. Sci. USA.* 93:10763–10768.

28. Blab, G. A., O. H. M. Lommerse, L. Cognet, G. S. Harms, and T. Schmidt. 2001. Two-photon excitation action cross-sections of the autofluorescent proteins. *Chem. Phys. Lett.* 350:71–77.

29. Callis, P. R. 1997. Two-photon-induced fluorescence. *Annu. Rev. Phys. Chem.* 48:271–297.

30. Macak, P., Y. Luo, P. Norman, and H. Agren. 2000. Electronic and vibronic contributions to two-photon absorption of molecules with multi-branched structures. *J. Chem. Phys.* 113:7055–7061.

31. Wiedenmann, J., A. Schenk, C. Röcker, A. Girod, K. D. Spindler, and G. U. Nienhaus. 2002. A far-red fluorescent protein with fast matu-ration and reduced oligomerization tendency from Entacmaea quadri-color (Anthozoa, Actinaria). *Proc. Natl. Acad. Sci. USA.* 99:11646–11651.

32. Nienhaus, K., B. Vallone, F. Renzi, J. Wiedenmann, and G. U. Nienhaus. 2003. Crystallization and preliminary x-ray diffraction anal-ysis of the red fluorescent protein eqFP611. *Acta Crystallogr. D Biol. Crystallogr.* 59:1253–1255.

33. Schenk, A., S. Ivanchenko, C. Röcker, J. Wiedenmann, and G. U. Nienhaus. 2004. Photodynamics of red fluorescent proteins studied by fluorescence correlation spectroscopy. *Biophys. J.* 86:384–394.

34. Hopt, A., and E. Neher. 2001. Highly nonlinear photodamage in two-photon fluorescence microscopy. *Biophys. J.* 80:2029–2036.

35. Zipfel, W. R., R. M. Williams, and W. W. Webb. 2003. Nonlinear magic: multiphoton microscopy in the biosciences. *Nat. Biotechnol.* 21:1369–1377.

36. Staudt, T., M. C. Lang, R. Medda, J. Engelhardt, and S. W. Hell. 2006. 2,2′-Thiodiethanol: a new water soluble mounting medium for high resolution optical microscopy. *Microsc. Res. Tech.* doi 10.1002/jemt.20396.

37. Schrader, M., K. Bahlmann, G. Giese, and S. W. Hell. 1998. 4Pi-confocal imaging in fixed biological specimens. *Biophys. J.* 75:1659–1668.

38. Baddeley, D., C. Carl, and C. Cremer. 2006. 4Pi microscopy de-convolution with a variable point-spread function. *Appl. Opt.* 45:7056–7064.